RSC Advances

PAPER

View Article Online
View Journal | View Issue

Cite this: *RSC Adv.*, 2017, 7, 50760

Hydrothermal synthesis and Cl_2 sensing performance of porous-sheets-like In_2O_3 structures with phase transformation†

Pei Li,* Chenglong Cai, Tiedong Cheng and Yanguo Huang

Received 13th September 2017
Accepted 22nd October 2017

DOI: 10.1039/c7ra10201a

rsc.li/rsc-advances

A facile hydrothermal route was employed to synthesize the porous-sheets-like In_2O_3 structures without any surfactant and template. The morphologies of the porous-sheets-like In_2O_3 structures consisted of many thin sheets with length of 40–120 nm, and the amount of Fe-doped significantly affected the overall morphologies and the phase transformation of In_2O_3. Furthermore, the formation mechanism of the porous-sheets-like In_2O_3 structure is investigated, which revealed that the doping of Fe plays a significant role in the self-assembled and oriented attachment mechanism of In_2O_3, and the phase transformation of In_2O_3 (the pure bcc-In_2O_3 was transformed into the pure rh-In_2O_3) also contributed to the formation of the porous-sheets-like In_2O_3 structure. Finally, the gas sensing characteristics of the products were studied. The results demonstrated that the sensor based on porous-sheets-like In_2O_3 structures (the coexistence of bcc-In_2O_3 and rh-In_2O_3) exhibited a much higher response (54.7 ± 5.3 for 5 ppm Cl_2) to Cl_2 than those pure bcc-In_2O_3 without Fe (S1) and pure rh-In_2O_3 (S5 and S6) samples, so the phase transformation influences on the gas sensing performance of In_2O_3. The porous-sheets-like In_2O_3 structures (S4) had the biggest surface area (42.5 m^2 g^{-1}), which contributed to the improvement of the gas sensing characteristics, the gas sensing mechanism were also studied.

Introduction

As n-type semiconductors with a wide band gap ($E_g = 3.6$ eV),[1] In_2O_3 has been proven to be a highly sensitive material for the detection of both reducing and oxidizing gases, such as trimethylamine ($N(CH_3)_3$),[2] C_2H_5OH,[3] HCHO,[4] CH_3COCH_3,[5] CO,[6] O_3,[7] H_2S,[8] Cl_2,[9] and NO_2,[10] *et al.* To enhance the functional properties of In_2O_3, the size, shape, surface chemistry, defect, and dispersion should be designed carefully. In particular, high surface area and nano-scale dimensions are the key factors to determine the gas response for application as gas sensors.[11–13] Up to now, In_2O_3 nano-/microstructure with different morphologies, such as nanocrystals,[14–16] 1D nanowires/nanobelts,[17,18] 2D thin films,[19,20] 2D nanosheets,[21] 3D hierarchical structures,[22–24] 3D nanotowers[25,26] have been developed. And 2D nanosheets are considered to be the most effective and promising candidates as gas sensors due to their unique structures with low density and high surface area.[27]

Meanwhile, doping is another simple and feasible approach to improve sensing performance by the way of catalytic effect, decreasing grain size, facilitating adsorption of gas, and so on.[28–30] For example, Zhang *et al.* found that the self-assembled hierarchical Au-loaded In_2O_3 hollow microspheres with superior ethanol sensing properties which is up to 9 times compared with the pure In_2O_3.[31] Ding *et al.* indicate that the Ag doped In_2O_3 (1%) is almost 23 times higher than that of the sensor based on pure In_2O_3 toward 1 ppm NO_2.[32] Moreover, the doping metal nanoparticles also can be integrated into the original hierarchical nanostructures, and the morphology would affect directly on the redox reaction at its surface by the doping elements. Wei *et al.* presented with the increase of Ce doping amount, the average sizes of the flower-like spheres were decrease, and the boundaries of as-prepared In_2O_3 microstructures gradually become more and more unconspicuous.[33] Li *et al.* found that by introduce of Fe, the flower-like structures (pure In_2O_3) collapsed into thin sheet-based structures (Fe doped In_2O_3).[21]

In_2O_3 has two phases: cubic In_2O_3 (bcc-In_2O_3) and rhombohedral In_2O_3 (rh-In_2O_3).[34,35] The stable form of In_2O_3 is body-centered cubic bixbyite-type crystal (bcc-In_2O_3), while the metastable corundum-type In_2O_3 (rh-In_2O_3) is rhombohedral.[36] The corundum In_2O_3 exhibits more stable conductivity than that of the cubic counterpart.[37] The rh-In_2O_3 transformed into the bcc-In_2O_3 phase under certain physical and chemical conditions, if the change of crystal structure can reduce the free energy of the system, which may affects the morphology and the gas sensing characteristic of In_2O_3.

School of Electrical Engineering and Automation, Jiangxi University of Science and Technology, Ganzhou 341000, China. E-mail: lipei8143706@163.com; Tel: +86-797-8312059

† Electronic supplementary information (ESI) available. See DOI: 10.1039/c7ra10201a

Herein, we report a facile hydrothermal route for the phase transformation of In_2O_3 structures (the pure bcc-In_2O_3 was transformed into the coexistence of bcc-In_2O_3 and rh-In_2O_3, then transformed into the pure rh-In_2O_3) with doped an appropriate amount of Fe. The morphologies of the porous-sheets-like In_2O_3 structures consisted of many thin sheets with length of 40–120 nm. The obtained nanomaterials were analyzed by scanning electron microscopy (SEM), transmission electron microscopy (TEM) characteristic techniques, ICP-MS instrument, and N_2 adsorption/desorption tests. The gas sensing properties of the resulting materials have also been investigated. The introduction of a small quantity of Fe in the reaction system was found to weigh heavily in the phase transformation of In_2O_3 structures, which affected the gas sensing properties of Cl_2.

Material and methods

Materials

The chemical reagents indium nitrate hydrate ($In(NO_3)_3\cdot4.5H_2O$), ferric nitrate hydrate ($Fe(NO_3)_3\cdot9H_2O$), polyvinyl pyrrolidone (PVP), ethylene glycol were of analytical grade and used without further purification. All the chemical reagents were purchased from Shanghai Chemical Co.

Synthesis

In a typical synthesis, 10 mL ethylene glycol was added into 30 mL distilled water under constantly strong stirring for 15 min. Then, 1.5 mmol of $In(NO_3)_3\cdot4.5H_2O$, 0.1500 g polyvinyl pyrrolidone, and different amounts of $Fe(NO_3)_3\cdot9H_2O$ were added into distilled water under constantly strong stirring. After being stirred for another 30 min, the solutions were transferred into 60 mL Teflon-lined stainless steel autoclaves. The autoclaves were heated at 140 °C for 12 h, and then cooled down to room temperature naturally. The reddish brown precipitates were separated by centrifugation, then washed with distilled water and anhydrous ethanol for several times, respectively, and dried at 80 °C for 6 h. Finally, porous-sheets-like Fe-doped In_2O_3 structures were obtained after a thermal treatment at 500 °C for 2 h. We refer to these samples as S1, S2, S3, S4, S5 and S6, representing pure In_2O_3, and the In/Fe molar ratios of 15 : 1, 12 : 1, 9 : 1, 7 : 1, and 5 : 1, respectively.

Characterization

The phase structure and purity of the as-synthesized products were examined by X-ray diffraction (XRD; X'pert PRO MPD, Philips, Eindhoven, The Netherlands) with Cu-Kα radiation ($\lambda = 1.5406$ Å) at 40 kV, 30 mA over the 2θ range 20–70°. The morphology of the obtained samples was investigated by using field emission scanning electron microscopy (FE-SEM; JSM-6701F, JEOL, Tokyo, Japan), and high resolution transmission electron microscopy (HRTEM; Tecnai F30G^2, FEI, Hillsboro, OR, USA) operated at 300 kV accelerating voltage. The chemical state is examined by high-resolution X-ray photoelectron spectroscopy (XPS) on a spectrometer (ESCALAB250Xi, Thermo Fisher Scientific, Waltham, MA, USA) with a monochromatic Al Kα source. An Agilent 7500a model ICP-MS system (Agilent Technologies, State of California, USA) was used for simultaneous multielement detection of Fe ions. The ICP-MS instrument is a Babington nebulizer with a double pass quartz spray chamber, the frequency RF generator is 10 MHz; the output power is 1220 W; the flow rate for Ar gas, auxiliary gas and nebuliser gas is 20 L min^{-1}, 0.9 L min^{-1} and 1–1.2 L min^{-1}, respectively; the sample uptake rate is 400 μL min^{-1}; the integration time is 0.1 s; and the wavelength is 206.200 nm. The porous characterization of the In_2O_3 structures was obtained by full analysis of N_2 adsorption/desorption tests (V-Sorb 2800P, Gold APP Instruments Corporation, Beijing, China). The AC impedance spectroscopy was measured with a precision impedance analyzer (4294A, Agilent, Santa Clara, CA, USA).

Gas sensor fabrication and measurements

The basic fabricated process is the same of reference.[38] The as-obtained In_2O_3 products were slightly grinded with α-terpineol in an agate mortar to form a gas sensing paste. The paste was coated on an alumina tube with Au electrodes and platinum wires, dried under IR light for several minutes in air, and then sintered at 500 °C for 2 h. A Ni–Cr alloy crossing alumina tube was used as a heating resistor which ensured both substrate heating and temperature control. In order to improve their stability, the gas sensors were aged at 300 °C for 240 h in air.

The gas sensing properties were tested by using a gas response instrument (HW-30A, Hanwei Ltd, Zhengzhou, China). The gas sensing properties of the In_2O_3 structures were tested in a glass test chamber, and the volume of the test chamber was 15 L. In the measuring electric circuit of the gas sensor, a load resistor was connected in series with a gas sensor. The circuit voltage V_c was 5 V, and the output voltage (V_{out}) was the terminal voltage of the load resistor R_L. The working temperature of the sensor was adjusted by varying the heating voltage V_h. When a given amount of tested gas was injected into the chamber, the resistance of the sensor changed. As a result, the output voltage changed. The gas response (S) is defined as eqn (1) and (2):

For an oxidizing gases:

$$\text{Response} = R_g/R_a \tag{1}$$

For a reducing gases:

$$\text{Response} = R_a/R_g \tag{2}$$

which R_g and R_a were the resistance values measured in an oxidizing or reducing atmosphere and air, respectively. For each sample, three sensors were made by the same fabrication process, each sensor was tested three times in the gas sensing testing process, and the gas response values in the text were the average value.

Results and discussion

Crystalline structure and morphology

Fig. 1a shows the XRD patterns of the pure In_2O_3 and Fe-doped In_2O_3 structures of S1, S2, S3, S4, S5 and S6 (from bottom to

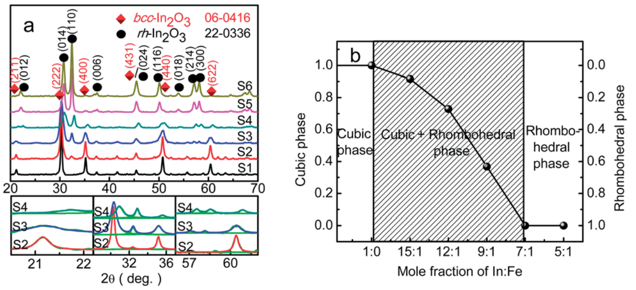

Fig. 1 (a) XRD patterns of pure In_2O_3 and Fe-doped In_2O_3 structures, and (b) relative concentration of the bcc-In_2O_3 phase with respect to the rh-In_2O_3 phase as a function of In/Fe molar ratios.

top). All the strong and sharp diffraction peaks marked by a diamond can be readily indexed to a cubic lattice [space group $Ia\bar{3}(206)$] of pure In_2O_3 according to the Joint Committee on Powder Diffraction Standards (JCPDS) data card no. 06-0416. All diffraction peaks marked by a circle can be readily indexed to a rhombohedral lattice [space group $R\bar{3}c(167)$] of pure In_2O_3 according to the JCPDS data card no. 22-0336. The XRD results show that with the increasing of Fe concentration, the pure bcc-In_2O_3 (S1) tended to be transformed into the coexistence of bcc-In_2O_3 and rh-In_2O_3 (S2, S3 and S4), and then transformed into the pure rh-In_2O_3 (S5 and S6).

According to the three Gaussian profiles fitting of the curves,[39] the intensities were determined for the bcc-In_2O_3 (400), bcc-In_2O_3 (440), and rh-In_2O_3 (012), rh-In_2O_3 (110) peaks. The relative phase concentration of the bcc-In_2O_3 phase in respect of the rh-In_2O_3 phase was estimated from profile fitting. The fractions of bcc-In_2O_3 (bcc) and rh-In_2O_3 (rh) phases were determined using the relations of eqn (3) and (4):

$$\mathrm{bcc} = \frac{I(400)_{\mathrm{bcc}} + I(440)_{\mathrm{bcc}}}{I(400)_{\mathrm{bcc}} + I(440)_{\mathrm{bcc}} + I(012)_{\mathrm{rh}} + I(110)_{\mathrm{rh}}} \tag{3}$$

$$\mathrm{rh} = (1 - \mathrm{bcc}) \tag{4}$$

As expected, the bcc-In_2O_3 phase fraction decreased with the decreasing of In/Fe molar ratios, as shown in Fig. 1b. Pure bcc-In_2O_3 phase was presence without Fe doped, while the coexistence of bcc-In_2O_3 and rh-In_2O_3 appeared by introducing of Fe (the In/Fe molar ratios were 15 : 1, 12 : 1 and 9 : 1), with further increasing of Fe content (the In/Fe molar ratios were 7 : 1 and 5 : 1), sole rh-In_2O_3 phase was presence. When the In/Fe molar ratio was 9 : 1 (S4), the bcc-In_2O_3 fraction was 36.8%, while the intensity of the rh-In_2O_3 reflection was 63.2%, indicating the presence of the coexistence of bcc-In_2O_3 and rh-In_2O_3. The degree of bcc-In_2O_3 remained unchanged throughout the two-phase region, only the relative amounts of the bcc-In_2O_3 and rh-In_2O_3 phases changed.

The cell parameters for bcc-In_2O_3 and rh-In_2O_3 and the size of the crystallites determined with the Scherrer formula were listed in Table 1. As can be seen, the above calculated lattice constants compare well with the literature values of $a = b = c =$ 10.118 Å (bcc-In_2O_3, JCPDS 06-0416), and $a = b =$ 5.487 Å, $c =$ 14.510 Å (rh-In_2O_3, JCPDS 22-0336). The size of the crystallites were 12.62, 11.97, 13.63, 10.84, 12.90, 13.11 nm for S1, S2, S3, S4, S5 and S6, respectively.

The concentration of Fe element in Fe-doped In_2O_3 structures was determined by using ICP-MS instrument, as shown in Table 1. The results indicate that the Fe^{3+} content (wt%) is very low in different amounts of Fe-doped samples, and the Fe^{3+} content increased with the decreasing of In/Fe molar ratios. The actual Fe^{3+} contents were 0, 1.20%, 1.49%, 1.97%, 2.46%, 3.41% (wt%) for S1, S2, S3, S4, S5 and S6, respectively.

Fig. 2a–f shows the SEM images of the pure bcc-In_2O_3, the coexistence of bcc-In_2O_3 and rh-In_2O_3 structures, and the pure rh-In_2O_3 structures. They indicate that Fe doping plays an important role in controlling the phase transformation and the morphology of In_2O_3. As shown in Fig. 2a, pure bcc-In_2O_3 consists of cubes with a size of 80–400 nm. Upon the introduction of Fe, the morphology of In_2O_3 changed into a mixture of cubes and porous thin sheets. With the increase of the amount of Fe doping, the number of cubes decreased, while the number of porous thin sheets increased, as shown in Fig. 2b–f. As depicted in Fig. 2b, very few porous thin sheets were present in S2 sample, with a size of 30–50 nm. Upon further increasing the Fe doping concentration (S3–S6), the amount and the size of cubes decreased sharply, while most of the In_2O_3 nanostructures consisted of porous thin sheets with larger size. When the In/Fe molar ratio was 9 : 1 (S4), as shown in Fig. 2d, a mass of porous thin sheets was appeared, with length of 40–120 nm, meanwhile, there existed very few cubes with length of 70 nm. On further increasing the Fe doping amount (S5 and S6), sole rh-In_2O_3 phase was presence. As can been seen from

Table 1 Cell parameters and the size of pure In_2O_3 and Fe-doped In_2O_3 structures, and the actual Fe^{3+} contents

	bcc-In_2O_3 (cell parameters)	rh-In_2O_3 (cell parameters)				
Sample	$a = b = c$ (Å)	$a = b$ (Å)	c (Å)	D (nm)	Theoretical In/Fe (molar ratio)	Actual Fe^{3+} contents (wt%)
S1	10.0956	—	—	12.62	—	—
S2	10.1109	5.4406	14.3219	11.97	15 : 1	1.20
S3	10.1201	5.4542	14.3207	13.63	12 : 1	1.49
S4	10.1268	5.4623	14.3560	10.84	9 : 1	1.97
S5	—	5.4590	14.3614	12.90	7 : 1	2.46
S6	—	5.4516	14.4008	13.11	5 : 1	3.41

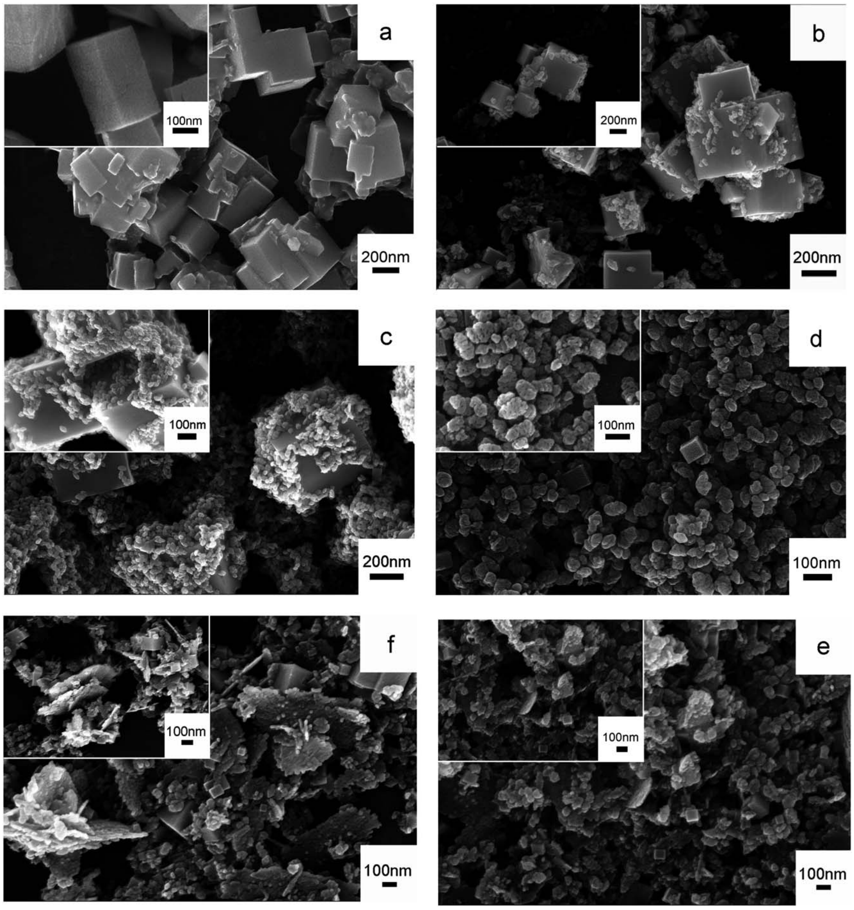

Fig. 2 SEM images of (a) S1, (b) S2, (c) S3, (d) S4, (e) S5 and (f) S6 (inset: high-magnification SEM images of S1–S6).

Fig. 2(e and f), some of the porous thin sheets agglomerated and grown into larger flakes, the size of the flakes increased further to 0.6–1 mm, which may destroy the morphology and affect the Cl_2 sensing performance of In_2O_3.

Transmission electron microscopy (TEM) is then employed to gain further insight into the porous-sheets-like Fe-doped In_2O_3 structures. Fig. 3a shows the TEM image of the porous-sheets-like In_2O_3 structures (S4), it shows that the diameter of the porous thin sheets is 50–100 nm, which is consistent with the value estimated in the SEM image (Fig. 2d). The corresponding HRTEM image (Fig. 3b) exhibits well-defined lattice fringes, and two kinds of lattice spacing can be observed. The lattice spacing of 0.291 nm corresponds to the (222) plane of bcc-In_2O_3, and the lattice spacing of 0.396 nm corresponds to the (012) plane of rh-In_2O_3.

Fig. 3c and d show the SAED patterns taken from the corresponding marked areas of A1 and A2, respectively. Fig. 3c indicates that the porous-sheets-like Fe-doped In_2O_3 grows along the [012] direction for rh-In_2O_3, while Fig. 3d demonstrates that the crystals grew along the [222] direction for bcc-In_2O_3, which is consistent with the values estimated from the HRTEM image (Fig. 3b). The EDX spectroscopy (Fig. 3e) shows that the porous-sheets-like Fe-doped In_2O_3 structures are elementally composed of In, Fe and O. The atomic ratio for In, Fe and O calculated from the EDX analysis was In/Fe/O = 31.01 : 1.66 : 67.31 (atomic ratio).

To further investigate the chemical state of the containing elements in the porous-sheets-like Fe-doped In_2O_3 structures (S4), the XPS data were collected and are presented in Fig. 4. The fully scanned spectra (Fig. 4a) shows the survey spectrum of Fe-doped In_2O_3, which indicates that the surface area of the synthesized material has elements of In, O, C and Fe. The C element is ascribed to adventitious carbon-based additives and the C 1s, whose banding energy peak locating at 284.6 eV, is used as reference for calibration.[16] The high resolution XPS spectrum of O 1s in Fig. 4b could be resolved to two Gaussian function peaks with the energy of 530.3 eV and 531.5 eV,[32] which are attributed to two kinds of oxygen species on the surface of the material. The O 1s core level spectrum recorded on the sample was a little asymmetric, because of α peaks are associated with lattice oxygen of In_2O_3 and the β peaks are arisen from the surface hydroxyl oxygen of In_2O_3.[31] The In 3d spectrum (shown in Fig. 4c) has two strong peaks at binding energy of 444.6 and 452.0 eV. They can be respectively indexed to the characteristic spin–orbit split states of In $3d_{5/2}$ and In $3d_{3/2}$ originated from In–O in In_2O_3 lattice,[40] indicating an In oxidation state of +3. Fig. 4d shows the high-resolution XPS spectrum of Fe 2p. It reveals the doublet Fe $2p_{3/2}$ and $2p_{1/2}$ with binding energies of 710.9 and 724.8 eV, respectively. Both peaks are accompanied by satellite structures with higher binding energy (approximately 8 eV), which is characteristic of the Fe^{3+} species.[41] The XPS analysis results show the

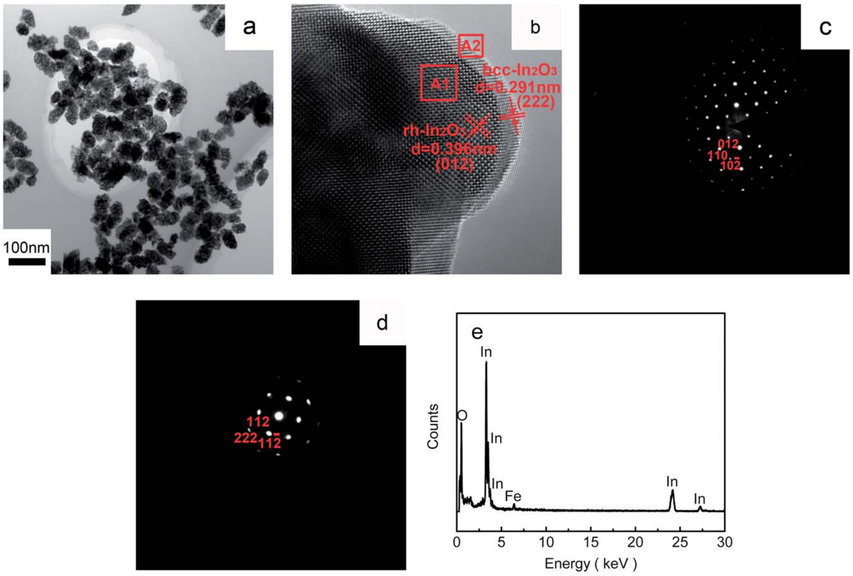

Fig. 3 (a) TEM and (b) HRTEM images of the porous-sheets-like Fe-doped In_2O_3 (S4); SAED patterns taken from the corresponding areas marked (c) A1 and (d) A2; and (e) the EDX spectrum of S4.

atomic ratio for In, Fe and O was In/Fe/O = 31.15 : 1.58 : 67.27 (atomic ratio). Hence, we have successfully synthesized Fe-doped In_2O_3 structures.

Determination of specific surface area and porosity

Fig. 5a and ESI Fig. A(1–5)† show the N_2 adsorption/desorption isotherms of the pure In_2O_3 and Fe-doped In_2O_3 structures. According to the IUPAC classification, the similar N_2 adsorption/desorption isotherms of the six samples can be classified as a type IV isotherm, with a hysteresis loop where desorption required definitively higher energy than adsorption. The isotherms of the porous-sheets-like Fe-doped In_2O_3 (S4) show a hysteresis loop at a relatively high pressure indicating the largest surface area. The amount of N_2 adsorbed was higher for S4 (459.8 $cm^3 g^{-1}$) than S1 (178.8 $cm^3 g^{-1}$), S2 (232.5 $cm^3 g^{-1}$), S3 (323.9 $cm^3 g^{-1}$), S5 (402.3 $cm^3 g^{-1}$), or S6 (366.3 $cm^3 g^{-1}$).

The pore size distributions are reported in Fig. 5b, apparently, the pore size of the porous-sheets-like Fe-doped In_2O_3 (S4)

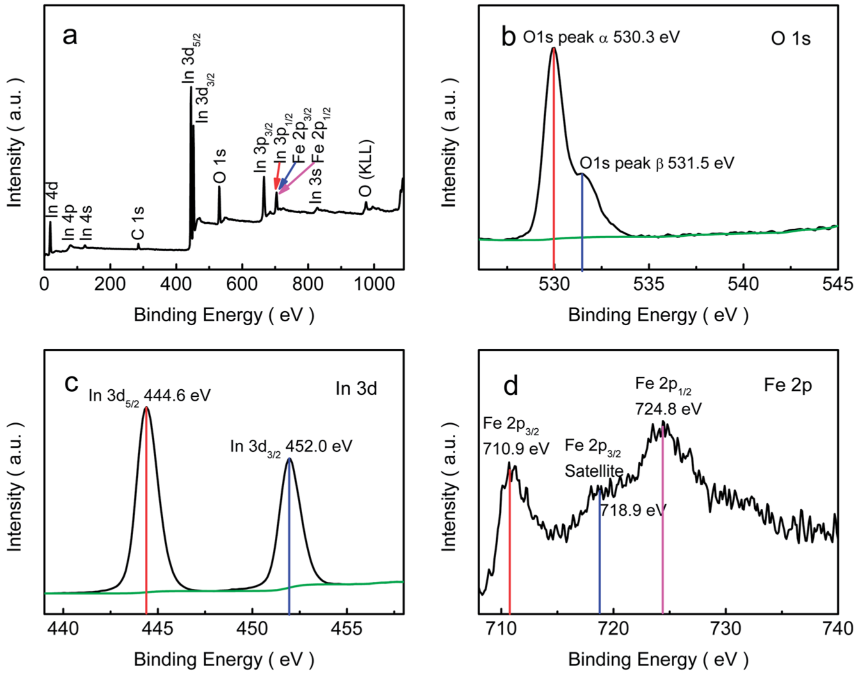

Fig. 4 XPS spectra of the porous-sheets-like Fe-doped In_2O_3 (S4): (a) fully scanned spectra, (b) O 1s, (c) In 3d, (d) Fe 2p.

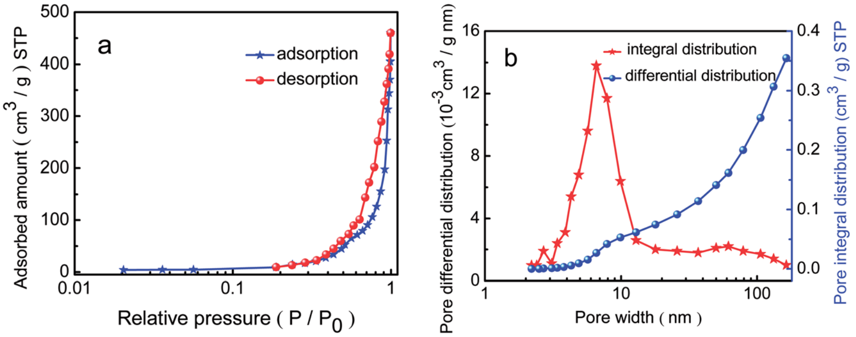

Fig. 5 N_2 adsorption–desorption curves (a) and the pore size distribution (b) of the porous-sheets-like Fe-doped In_2O_3 (S4).

concentrate between 2 and 10 nm. The results suggest that a small pore size distribution and uniform pore structure were obtained. The steepness of desorption branch verified the uniformity of the pore diameter with narrow distribution. Moreover, it is evident that both small and large pore diameters were in the mesopore region. The pores in the porous-sheets-like Fe-doped In_2O_3 structure also has been proved by the SEM image (Fig. 2d) and the TEM image (Fig. 3a).

Phase transformation mechanism and formation mechanism of the porous-sheets-like Fe-doped In_2O_3 structures

We found that the concentration of Fe-doped determine both crystal phase and morphology of In_2O_3 in the final products.

According to some literatures,[38,42,43] the two phases of In_2O_3 (bcc-In_2O_3 and rh-In_2O_3) will transform to each other when sufficient energy is made available, although the rh-In_2O_3 is the so-called metastable states and the bcc-In_2O_3 is stable states. In certain physical and chemical conditions, if the change of crystal structure reduced the free energy of the system, the polymorphism transformation was inevitable. The added Fe^{3+} ions changed the growth rate in the crystal plane of bcc-In_2O_3 phase, so the displacive transformation of bcc-In_2O_3 structure happened and transformed into the rh-In_2O_3 phase. In result, some bcc-In_2O_3 phase is transformed into the rh-In_2O_3 phase, with further increasing of Fe content, sole rh-In_2O_3 phase was presence. XRD patterns of the samples obtained at different In/Fe molar ratios of 0, 15 : 1, 12 : 1, 9 : 1, 7 : 1, and 5 : 1 reveals the tendency of phase transformation, which is shown in Fig. 1a. Without Fe, the obtained sample was bcc-In_2O_3 (S1), when In/Fe molar ratios was increased to 15 : 1–9 : 1 (S2, S3 and S4), the prepared samples were mixture of bcc-In_2O_3 and rh-In_2O_3, and upon the increase of the amount of Fe, relative amounts of the rh-In_2O_3 increased. Pure rh-In_2O_3 was obtained when In/Fe molar ratios reached to 7 : 1 and 5 : 1 (S5 and S6).

The formation mechanism of the porous sheets-like Fe-doped In_2O_3 structures was also proposed. The whole growth process was illustrated in the scheme of Fig. 6. The concentration of Fe-doped also determine the morphology of In_2O_3, and the corresponding SEM images are shown in Fig. 2a–f. Without Fe (S1), cubes were formed. By increasing the In/Fe molar ratios to 15 : 1 (S2), some porous thin sheets appeared with large number of cubic. Upon further increasing the Fe doping concentration of (S3–S6), the amount of cubes decreased sharply, while most of the In_2O_3 sample consisted of porous thin sheets. However, more Fe resulted in the agglomeration of the porous thin sheets (S5 and S6). These experimental results reveal that the amount of Fe affects the morphology.

Without Fe, the obtained sample was pure bcc-In_2O_3, the bcc-In_2O_3 was simply enclosed by {001} faces because these faces have the slowest growth rate and lowest surface energy. The cubic shape is consistent with the cubic crystal structure of In_2O_3.[44] In the In_2O_3 cubic structure, the {001} family of planes contain three equivalent planes, (100), (010), and (001), which are perpendicular to the three directions [100], [010], and [001], respectively. The In_2O_3 nanocrystallites grow in all three directions at an equal speed.[45,46] Consequently, the cubic morphology of the product enclosed with crystal faces of {001} is obtained (S1 in Fig. 2a).

After the doping of Fe, the bcc-In_2O_3 structure was transformed into the rh-In_2O_3 phase. During the hydrolyzation process of rh-In_2O_3, the generation rate of the $In(OH)_3$ nanoparticles was slow in solution. The relative slow generation rate of $In(OH)_3$ is favorable for the subsequent growth of 2D nanosheets-like-structures along with the determined direction. Then, these primary nanoparticles self-assembly by oriented attachment aggregated into sheets (S2–S6 in Fig. 2b–f). As the

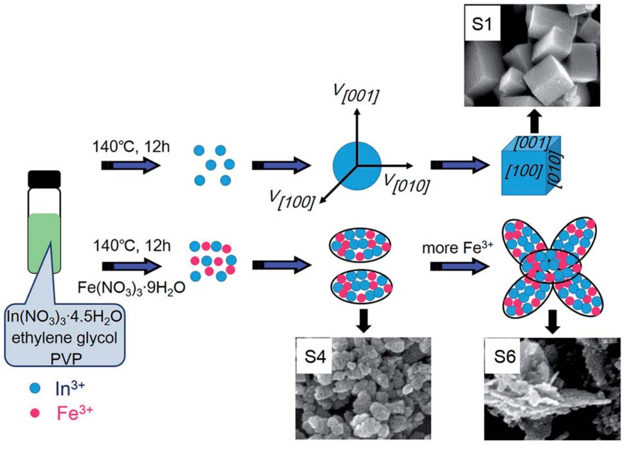

Fig. 6 Formation schematic of the porous-sheets-like Fe-doped In_2O_3 structures.

larger ionic radius induces the higher diffusion barrier, the diffusion coefficient is lower with a bigger radius.[47] Because of the larger size of indium ions (In^{3+}: 80 pm, Fe^{3+}: 64 pm), the diffusion of iron ions through the In_2O_3–Fe interface is faster than that of indium ions to the In_2O_3–Fe interface, the gradual inward diffusion of iron ions leads to the increase of the overall size of the porous thin sheets. So, with increasing of Fe-added amount, the diameter of porous thin sheets increased, as shown in Fig. 2b–d. With further increasing of Fe-doped amount (S5 and S6), the diameter of porous thin sheets continues to increase, some of the porous thin sheets agglomerated and grown into larger flakes, as shown in Fig. 2e and f.

Gas sensing properties

Fig. 7 displays the plots of gas response *versus* the gas concentration when the sensors based on the samples with different amounts of Fe were exposed to Cl_2 with the concentration ranging from 5 to 100 ppm at 300 °C. The results show that the response increased for each sensor with the increasing of the concentration of Cl_2. The sensors based on Fe-doped structures exhibit a much higher response than those based on the pure In_2O_3 structures (S1), and the In/Fe molar ratio 9 : 1 (S4) sensor has the highest response. The appropriate addition of Fe would be beneficial to the improvement of the gas sensing properties, but superabundant addition may reduce the available adsorption sites and worse the gas sensing properties. It reveals that the porous-sheets-like Fe-doped In_2O_3 structures (S4) sensor has the highest response which can reach 54.7 ± 5.3, 180.3 ± 18.8, 517.3 ± 52.2, 1186.8 ± 117.1, 1752.5 ± 169.9 for 5, 10, 30, 50, and 100 ppm Cl_2, respectively. Therefore, the following study of the selectivity was focused on the S4 sensor.

The single point surface area was clearly the largest for S4 (42.5 $m^2\ g^{-1}$) than S1 (18.3 $m^2\ g^{-1}$), S2 (24.6 $m^2\ g^{-1}$), S3 (28.1 $m^2\ g^{-1}$), S5 (36.9 $m^2\ g^{-1}$), or S6 (33.7 $m^2\ g^{-1}$), which is shown in Fig. 7. The increase in surface area for S4 is due to its porous-sheets-like structural features, which was evidenced by the SEM images, TEM images and the pore size distribution (BET). With the support of the pores in the surface of the porous-sheets-like structures, the BET specific surface became larger. The larger the surface area, the easier the mass transport of Cl_2 in the material. So, the porous-sheets-like Fe-doped In_2O_3 (S4) possess excellent gas sensing characteristics.

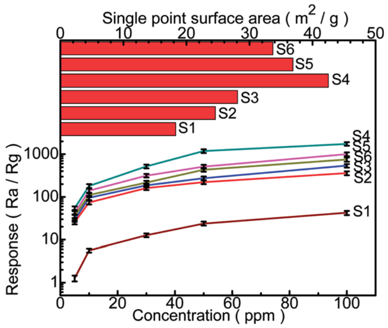

Fig. 7 Gas response of sensors based on samples with different amounts of Fe doping, exposed to Cl_2 at concentrations ranging from 5 to 100 ppm at 300 °C, and the single point surface area of S1–S6. The error bars show the standard deviation between the three gas sensing tests of the three sensors made by the same fabrication process.

As we know, the gas-sensing properties of a sensor have an important relationship with the operating temperature. To find the optimum detection temperature of the sensors based on the porous-sheets-like Fe-doped In_2O_3 structures (S4), we investigated the sensor responses to 50 ppm Cl_2 at the operating temperature from 80 °C to 300 °C, as indicated in Fig. 8a. From which it can be obviously observed accompanied by the increasing operating temperature, the response values of the sensor increasing. It is mainly owing to activation energy barrier of chem-sorption and surface reactions overcome by the increasing thermal energy.[48] Such behaviour can be understood by considering the role of the kind of adsorption oxygen and the characteristic of Cl_2, the oxygen adsorption depends on the particle size, large specific area of the material, and the operating temperature of the sensor.[49] In_2O_3 is typical of the performance of a surface-controlled gas sensor. With increasing the temperature in ambience, the state of oxygen adsorbed on the surface of the as-prepared porous-sheets-like In_2O_3 structures material. The species of physical adsorption oxygen (O_2^- (ads)) or chemical adsorption oxygen (O^- (ads), O_2^{2-} (ads)) depends on the material,[50,51] while the surface adsorbed oxygen changes with the change of the operating temperature. When the working temperature is lower (<160 °C), most of the adsorbed oxygen is O_2^- (ads), indicated as physical adsorption; with the increase of the working temperature (160 °C < T < 300 °C), the O_2^- (ads) is transformed into the O^- (ads), showed as the chemical adsorption. The reaction rate of chemical oxygen adsorption (O^- (ads)) is higher than the physical adsorption (O_2^- (ads)).[52] As the amount of adsorbed oxygen increase with the operation temperature, the responses increase with operating temperature. When the Cl_2 was injected in the test chamber, the Cl_2 was adsorbed on the surface of the gas sensing materials, and then reacted with the oxygen adsorbed on the surface of the In_2O_3, leading to an increase in sensor resistance.

Moreover, it can be seen from Fig. 8b that the response increased with the operating temperature, when the operating temperature was 300 °C, the response was 1186.8 ± 117.1 for 50 ppm Cl_2. Therefore, we chose 300 °C as the operating temperature for the subsequent detections of the porous-sheets-like Fe-doped In_2O_3 structures.

Under the optimum operating temperature of 300 °C, the typical response/recovery curve of the porous-sheets-like Fe-doped In_2O_3 structures (S4) to various concentrations of Cl_2 (5–100 ppm) is displayed in Fig. 9a. This response transient indicated that the interaction between the porous-sheets-like Fe-doped In_2O_3 structures and Cl_2 was reversible with a fast equilibration time. The porous-sheets-like Fe-doped In_2O_3 structures (S4) exhibited excellent response in the range of 5–100 ppm Cl_2. With the increase of the Cl_2 concentration, the responses of the sensor become higher. At low concentration, such as 5 ppm, the sensors have good response ($S = 54.7 \pm 5.3$), indicating that a high gas response can be achieved in detecting low concentration Cl_2 using the porous-sheets-like Fe-doped In_2O_3 structures as sensing material. Furthermore, the sensor

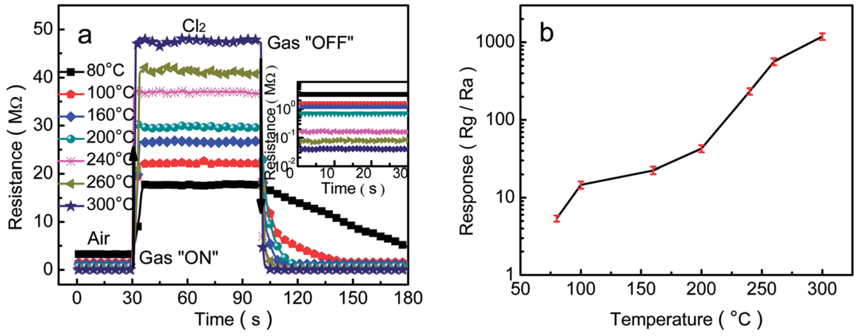

Fig. 8 Gas response of sensor as a function of sample (a) typical response and recovery curve of the sensor based on the porous-sheets-like Fe-doped In_2O_3 structures (S4) exposed to 50 ppm Cl_2 at different working temperatures. (b) Temperature dependence of the sensor gas response to 50 ppm Cl_2. The error bars mean the standard deviation between the three times in the gas sensing testing of all the three sensors made by the same fabricated process.

showed a quick response and short recovery time. When exposed to 50 ppm Cl_2, the response and recovery time (defined as the time required to reach 90% of the final equilibrium value) is 2 s and 5 s, respectively, indicating the fast response and quick recovery of the porous-sheets-like Fe-doped In_2O_3 structures (S4) sensor, as shown in Fig. 9b.

The selectivity is a very important parameter of a gas sensor, the response of a sensor has a significant relationship with the adsorption and reaction of gas molecules on the materials surface.[53] Fig. 10 displays the histogram of the response of porous-sheets-like Fe-doped In_2O_3 structures (S4) based sensors to eight kinds of tested gases with a concentration of 50 ppm at 300 °C. The tested gases or vapours include toluene, acetone, ammonia, nitrogen dioxide, hydrogen sulfide, formaldehyde, and gasoline, respectively. The porous-sheets-like Fe-doped In_2O_3 structures (S4) sensor showed the highest response to Cl_2 (1186.8 ± 117.1), while its response to toluene, acetone, ammonia, nitrogen dioxide, hydrogen sulfide, formaldehyde, gasoline is 3.5 ± 0.3, 1.8 ± 0.1, 5.3 ± 0.5, 101.9 ± 11.2, 8.1 ± 0.8, 7.2 ± 0.7, and 6.4 ± 0.6, respectively. Clearly, the gas response to Cl_2 is significantly higher than that to the other tested gases, with a magnitude about 11.6–659.3 times greater to 50 ppm Cl_2 than that for the other tested gases under the same concentration. The above results indicates the porous-sheets-like Fe-doped In_2O_3 structures (S4) sensor has good selectivity to Cl_2 at 300 °C.

The stability of the porous-sheets-like Fe-doped In_2O_3 structures (S4) sensor to Cl_2 with a concentration of 50 ppm at 300 °C is shown in Fig. 11. The sensor was stored in air and kept working at 300 °C for subsequent sensing property tests after the first measurement. The results show that the response decreased over time, but the response was still very high even after 30 days, indicating a good stability in a natural environment.

Based on the above results, it is reasonable to believe that the porous-sheets-like Fe-doped In_2O_3 structures (S4) sensor is potentially applicable to detecting the Cl_2 concentration in our living environment, due to its high response, short response–recovery time, excellent selectivity and good stability.

Gas sensing mechanism

The gas sensing mechanism of the porous-sheets-like Fe-doped In_2O_3 structures was also discussed.

Firstly, the as-prepared porous-sheets-like In_2O_3 structures adsorbs oxygen from the air and captures free electrons from the conduction band which causes the chemisorbed negatively charged oxygen ions (O_2^-, O^- and O^{2-}) and electron-depleted region generated on the surface, thus leading to the formation of a thick space charge layer and an increase of surface band bending. However, only O_2^-, O^- could be formed when

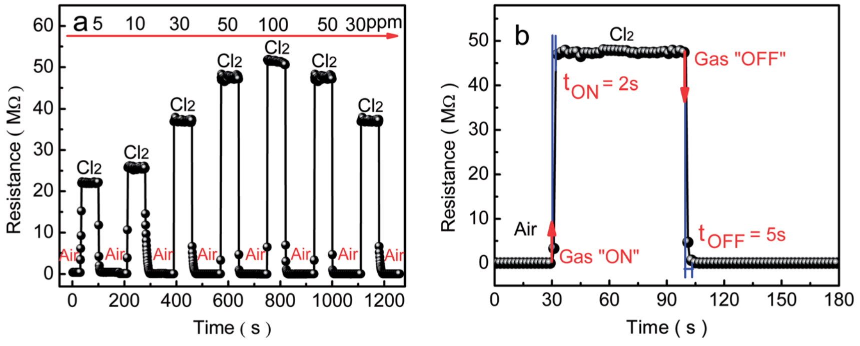

Fig. 9 Gas response of the sensor based on the porous-sheets-like Fe-doped In_2O_3 structures (S4) exposed to Cl_2 at (a) concentrations ranging from 5 to 100 ppm at 300 °C and (b) 50 ppm.

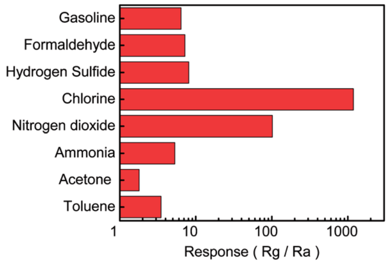

Fig. 10 Selectivity of the porous-sheets-like Fe-doped In_2O_3 structures (S4) sensor to Cl_2 with a concentration of 50 ppm at 300 °C.

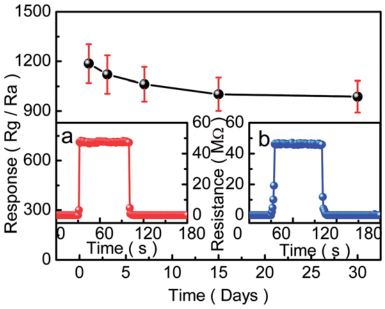

Fig. 11 Stability of the porous-sheets-like Fe-doped In_2O_3 structures (S4) sensor to Cl_2 with a concentration of 50 ppm at 300 °C. (Inset: (a) gas response of the sensor for the first day (b) the 30th) the error bars mean the standard deviation between the three times in the gas sensing testing of all the three sensors made by the same fabrication process.

the temperature is lower than 300 °C.[54] Then it would result an increase on the resistance. These adsorption processes can be expressed as eqn (5) and (7).

$$O_2\ (gas) \Leftrightarrow O_2\ (ads) \tag{5}$$

$$O_2\ (ads) + e^- \rightarrow O_2^-\ (ads) \tag{6}$$

$$O_2^-\ (ads) + e^- \rightarrow 2O^-\ (ads) \tag{7}$$

When Cl_2 is introduced in this condition, as the highly reactive oxidizing gas, Cl_2 intensely capture electrons from the conduction band due to its higher electrophilic property, and reacted with the adsorbed oxygen species leading to the formation of adsorbed Cl^- (ads), while the electron-depleted region is then further thickened. As a result, the resistance of the In_2O_3 sensor greatly increases. For the resistance increase, Cl_2 molecule is negatively adsorbed on In_2O_3 to attract electrons from In_2O_3 (eqn (8)). On the other hand, Cl_2 molecule is substituted with adsorbed oxygen (O^{2-}(ads)) or lattice oxygen (O_x^{2-}) to release electrons into In_2O_3 for resistance decrease (eqn (9) and (10)).[55]

Resistance increase:

$$\frac{1}{2}Cl_2\ (gas) + e^- \rightarrow Cl^-\ (ads) \tag{8}$$

Resistance decrease:

$$O^{2-}\ (ads) + \frac{1}{2}Cl_2\ (gas) \rightarrow Cl^-(ads) + \frac{1}{2}O_2\ (gas) + e^- \tag{9}$$

or

$$O_x^{\ 2-} + \frac{1}{2}Cl_2\ (gas) \rightarrow Cl_x^{\ -} + \frac{1}{2}O_2\ (gas) + e^- \tag{10}$$

The above reactions decrease the carrier concentration and electron mobility on the sensor surface, which led to the increase of depletion layer width accompanied by an increase in resistance. The electron transfer between In_2O_3 and Fe also led to the formation of an accumulation layer on the surface of the porous-sheets-like Fe-doped In_2O_3 structures. On the other hand, the trapped electrons were released to the porous-sheets-like Fe-doped In_2O_3 structures by Cl_2 after the supply of Cl_2 was stopped, leading to a decrease of the resistance.

The enhanced sensing performance of the porous-sheets-like Fe-doped In_2O_3 structures can be ascribed to its large BET surface area. The porous-sheets-like Fe-doped In_2O_3 structures could provide more available active surface areas because of the unique porous microstructure and its own good physicochemical properties, thus enhancing the reaction between Cl_2 and the adsorbed oxygen at the optimum operating temperature of sensor. The porous microstructure also increased the BET surface area of Fe-doped In_2O_3 structures. As the porous-sheets-like Fe-doped In_2O_3 structures (S4) had the largest BET surface area (42.5 $m^2\ g^{-1}$), the sensor could absorb more Cl_2, the resistance's increasing and the resistance's decreasing became more notable, which can enhance its sensing performance.

In order to observe clearly dielectric response of the pure In_2O_3 and Fe-doped In_2O_3, AC impedance spectroscopy of In_2O_3/Fe sensor with different amounts of Fe doping in the frequency range of 100 Hz to 10 MHz at 300 °C (50 ppm Cl_2) are shown in Fig. 12. Upon the introduction of Fe, the diameter of semicircle of AC impedance spectroscopy enlarged, the impedance increased, too. The AC impedance spectroscopy of the sensor based on S4 shows the largest semicircle (the inserted in Fig. 12), which is far larger than the value of sensors based on S1, S2, S3, S5, and S6. This is mainly due to the largest surface area of the S4 sample, which leading to the largest

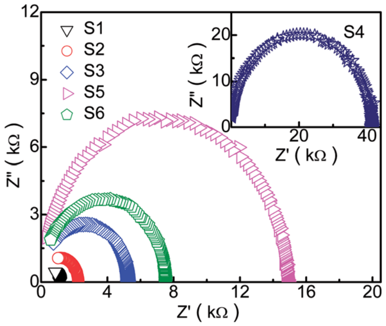

Fig. 12 AC impedance spectroscopy of S1, S2, S3, S4 (inset), S5 and S6 based sensors.

resistance. With further increasing of Fe doping concentration, the surface area decrease, and the resistance declined. It agrees well with SEM images, N_2 adsorption/desorption curve and the BET surface area value. More details of the enhancing effect of the porous-sheets-like Fe-doped In_2O_3 structures on sensing properties need further investigation.

Conclusions

A facile hydrothermal route for the phase transformation of In_2O_3 structures (the pure bcc-In_2O_3 was transformed into the pure rh-In_2O_3) without any surfactant and template was discussed. SEM images showed the molar ratio of In/Fe profoundly affected the morphologies of the In_2O_3/Fe composites and the porous-sheets-like Fe-doped In_2O_3 structures was obtained when the molar ratio of In/Fe was 9 : 1 (S4). A possible growth mechanism of the porous-sheets-like Fe-doped In_2O_3 structures has been proposed. The gas sensing measurements demonstrated that the porous-sheets-like Fe-doped In_2O_3 structures (S4) sensor exhibited the highest response of 54.7 ± 5.3 for 5 ppm Cl_2 at 300 °C. That is due to the large specific surface area of the porous-sheets-like Fe-doped In_2O_3 structures. Moreover, the sensor showed quick response–recovery behaviour, excellent selectivity and stability. Therefore, it is expected that this facile route to prepare the porous-sheets-like Fe-doped In_2O_3 structures would be an ideal candidate for applications in Cl_2 sensors.

Conflicts of interest

There are no conflicts to declare.

Acknowledgements

This work was supported by the Science Foundation of Department of Education of JiangXi Province (No. GJJ150677), the National Natural Science Foundation (61463020).

Notes and references

1 F. L. Gong, H. Z. Liu, C. Y. Liu, Y. Y. Gong, Y. H. Zhang, E. Meng and F. Li, 3D hierarchical In_2O_3 nanoarchitectures consisting of nanocuboids and nanosheets for chemical sensors with enhanced performances, *Mater. Lett.*, 2016, **163**, 236–239.

2 C. S. Lee, I. D. Kim and J. H. Lee, Selective and sensitive detection of trimethylamine using ZnO-In_2O_3 composite nanofibers, *Sens. Actuators, B*, 2013, **181**, 463–470.

3 F. Huang, W. Yang, F. He and S. T. Liu, Controlled synthesis of flower-like In_2O_3 microrods and their highly improved selectivity toward ethanol, *Sens. Actuators, B*, 2016, **235**, 86–93.

4 W. H. Zhang, W. C. Zhang, B. Chen, R. Shao, R. F. Guan, W. D. Zhang, Q. F. Zhang, G. H. Hou and L. Yue, Controllable biomolecule-assisted synthesis and gas sensing properties of In_2O_3 micro/nanostructures with double phases, *Sens. Actuators, B*, 2017, **239**, 270–278.

5 M. Karmaoui, S. G. Leonardi, M. Latino, D. M. Tobaldi, N. Donato, R. C. Pullar, M. P. Seabra, J. A. Labrincha and G. Neri, Pt-decorated In_2O_3 nanoparticles and their ability as a highly sensitive (<10 ppb) acetone sensor for biomedical applications, *Sens. Actuators, B*, 2016, **230**, 697–705.

6 Y. T. Yua, S. M. Majhia and H. G. Song, Synthesis and gas sensing properties of Au@In_2O_3 core-shell nanoparticles, *Procedia Eng.*, 2016, **168**, 227–230.

7 A. Gurlo, N. Bârsan, M. Ivanovskaya, U. Weimar and W. Göpel, In_2O_3 and MoO_3-In_2O_3 thin film semiconductor sensors: interaction with NO_2 and O_3, *Sens. Actuators, B*, 1998, **47**, 92–99.

8 J. C. Tu, N. Li, X. Y. Lai, Y. Chi, Y. J. Zhang, W. Wang, X. T. Li, J. X. Li and S. L. Qiu, H_2S-sensing properties of Pt-doped mesoporous indium oxide, *Appl. Surf. Sci.*, 2010, **256**, 5051–5055.

9 P. Li, H. Q. Fan and Y. Cai, In_2O_3/SnO_2 heterojunction microstructures: facile room temperature solid-state synthesis and enhanced Cl_2 sensing performance, *Sens. Actuators, B*, 2013, **185**, 110–116.

10 B. X. Xiao, S. L. Song, P. Wang, Q. Zhao, M. Y. Chuai and M. Z. Zhang, Promoting effects of Ag on In_2O_3 nanospheres of sub-ppb NO_2 detection, *Sens. Actuators, B*, 2017, **241**, 489–497.

11 S. F. Chen, X. L. Yu, H. Y. Zhang and W. Liu, Preparation, characterization and activity evaluation of heterostructure In_2O_3/$In(OH)_3$ photocatalyst, *J. Hazard. Mater.*, 2010, **180**, 735–740.

12 H. L. Tian, H. Q. Fan, M. M. Li and L. T. Ma, Zeolitic imidazolate framework coated ZnO nanorods as molecular sieving to improve selectivity of formaldehyde gas sensor, *ACS Sens.*, 2016, **1**, 243–250.

13 N. Song, H. Q. Fan and H. L. Tian, PVP assisted in situ synthesis of functionalized graphene/ZnO (FGZnO) nanohybrids with enhanced gas-sensing property, *J. Mater. Sci.*, 2015, **50**, 2229–2238.

14 A. Ilin, M. Martyshov, E. Forsh, P. Forsh, M. Rumyantseva, A. Abakumov, A. Gaskov and P. Kashkarov, UV effect on NO_2 sensing properties of nanocrystalline In_2O_3, *Sens. Actuators, B*, 2016, **231**, 491–496.

15 B. X Xiao, F. Wang, C. B. Zhai, P. Wang, C. H. Xiao and M. Z. Zhang, Facile synthesis of In_2O_3 nanoparticles for sensing properties at low detection temperature, *Sens. Actuators, B*, 2016, **235**, 251–257.

16 L. T. Ma, H. Q. Fan, H. L. Tian, J. W. Fang and X. Z. Qian, The n-ZnO/n-In_2O_3 heterojunction formed by a surface-modification and their potential barrier-control in methanal gas sensing, *Sens. Actuators, B*, 2016, **222**, 508–516.

17 N. Singh, A. Ponzoni, E. Comini and P. S. Lee, Chemical sensing investigations on Zn-In_2O_3 nanowires, *Sens. Actuators, B*, 2012, **171–172**, 244–248.

18 S. Parka, G. Suna, H. Kheela, W. Leeb, S. Leec, S. Choid and C. Lee, Synergistic effects of codecoration of oxide nanoparticles on the gas sensing performance of In_2O_3 nanorods, *Sens. Actuators, B*, 2016, **227**, 591–599.

19 J. Rombach, A. Papadogianni, M. Mischo, V. Cimalla, L. Kirste, O. Ambacher, T. Berthold, S. Krischok, M. Himmerlich, S. Selve and O. Bierwagen, The role of surface electron accumulation and bulk doping for gas-sensing explored with single-crystalline In_2O_3 thin films, *Sens. Actuators, B*, 2016, **236**, 909–916.

20 Y. Y. Wang, G. T. Duan, Y. D. Zhu, H. W. Zhang, Z. K. Xu, Z. F. Dai and W. P. Cai, Room temperature H2S gas sensing properties of In_2O_3 micro/nanostructured porous thin film and hydrolyzation-induced enhanced sensing mechanism, *Sens. Actuators, B*, 2016, **228**, 74–84.

21 P. Li, Y. Cai and H. Q. Fan, Porous thin sheet-based α-Fe_2O_3-doped In_2O_3 structures: hydrothermal synthesis and enhanced Cl_2 sensing performance, *RSC Adv.*, 2013, **3**, 22239–22245.

22 M. Gholami, A. A. Khodadadi, A. A. Firooz and Y. Mortazavi, In_2O_3-ZnO nanocomposites: High sensor response and selectivity to ethanol, *Sens. Actuators, B*, 2015, **212**, 395–403.

23 P. Song, D. Han, H. H. Zhang, J. Li, Z. X. Yang and Q. Wang, Hydrothermal synthesis of porous In_2O_3 nanospheres with superior ethanol sensing properties, *Sens. Actuators, B*, 2014, **196**, 434–439.

24 S. Zhang, P. Song, J. Li, J. Zhang, Z. X. Yang and Q. Wang, Facile approach to prepare hierarchical Au-loaded In_2O_3 porous nanocubes and their enhanced sensing performance towards formaldehyde, *Sens. Actuators, B*, 2017, **241**, 1130–1138.

25 S. T. Jean and Y. C. He, Growth mechanism and photoluminescence properties of In_2O_3 nanotowers, *Cryst. Growth Des.*, 2010, **10**, 2104–2110.

26 Y. J. Huang, K. Yu, Z. Xu and Z. Q. Zhu, Novel In_2O_3 nanostructures fabricated by controlling the kinetics factor for field emission display, *Phys. E*, 2011, **43**, 1502–1508.

27 H. X. Dong, Y. Liu, G. H. Li, X. W. Wang, D. Xu, Z. H. Chen, T. Zhang, J. Wang and L. Zhang, Hierarchically rosette-like In_2O_3 microspheres for volatile organic compounds gas sensors, *Sens. Actuators, B*, 2013, **178**, 302–309.

28 J. Zhao, T. L. Yang, Y. P. Liu, Z. Y. Wang, X. W. Li, Y. F. Sun, *et al.*, Enhancement of NO_2 gas sensing response based on ordered mesoporous Fe-doped In_2O_3, *Sens. Actuators, B*, 2014, **191**, 806–812.

29 Y. L. Wang, X. B. Cui, Q. Y. Yang, J. Liu, Y. Gao and P. Sun, Preparation of Ag-loaded mesoporous WO_3 and its enhanced NO_2 sensing performance, *Sens. Actuators, B*, 2016, **225**, 544–552.

30 Y. Qu, H. Wang, H. Chen, M. M. Han and Z. D. Lin, Synthesis, characterization and sensing properties of mesoporous C/SnO_2 nanocomposite, *Sens. Actuators, B*, 2016, **228**, 595–604.

31 S. Zhang, P. Song, H. H. Yan and Q. Wang, Self-assembled hierarchical Au-loaded In_2O_3 hollow microspheres with superior ethanol sensing properties, *Sens. Actuators, B*, 2016, **231**, 245–255.

32 M. D. Ding, N. Xie, C. Wang, X. Y. Kou, H. Zhang, L. L. Guo, Y. F. Sun, X. H. Chuai, Y. Gao, F. M. Liu, P. Sun and G. Y. Lu, Enhanced NO_2 gas sensing properties by Ag-doped hollow urchin-like In_2O_3 hierarchical nanostructures, *Sens. Actuators, B*, 2017, **252**, 418–427.

33 D. D. Wei, Z. S. Huang, L. W. Wang, X. H. Chuai, S. M. Zhang and G. Y. Lu, Hydrothermal synthesis of Ce-doped hierarchical flower-like In_2O_3 microspheres and their excellent gas-sensing properties, *Sens. Actuators, B*, 2017, DOI: 10.1016/j.snb.2017.07.162.

34 S. W. Shu, D. B. Yu, Y. Wang, F. Wang, Z. R. Wang and W. Zhong, Thermal-induced phase transition and assembly of hexagonal metastable In_2O_3 nanocrystals: a new approach to In_2O_3 functional materials, *J. Cryst. Growth*, 2010, **312**, 3111–3116.

35 X. Q. Wang, M. F. Zhang, J. Y. Liu, T. Luo and Y. T. Qian, Shape- and phase-controlled synthesis of In_2O_3 with various morphologies and their gas-sensing properties, *Sens. Actuators, B*, 2009, **137**, 103–110.

36 W. H. Zhang and W. D. Zhang, Biomolecule-assisted synthesis and gas-sensing properties of porous nanosheet-based corundum In_2O_3 microflowers, *J. Solid State Chem.*, 2012, **186**, 29–35.

37 W. H. Zhang and W. D. Zhang, Synthesis and optical properties of nanosheet-based rh-In_2O_3 microflowers by triethylene glycol-mediated solvothermal process, *J. Phys. Chem. Solids*, 2013, **74**, 1271–1274.

38 P. Li, H. Q. Fan, Y. Cai, M. M. Xu, C. B. Long, M. M. Li, S. H. Lei and X. W. Zou, Phase transformation (Cubic to Rhombohedral): great effects on NO_2 sensing performance of Zn-doped flower-like In_2O_3 structures, *RSC Adv.*, 2014, **4**, 15161–15170.

39 H. Q. Fan and H. E. Kim, Perovskite stabilization and electromechanical properties of polycrystalline lead zinc niobate-lead zirconate titanate, *J. Appl. Phys.*, 2002, **91**, 317–322.

40 J. Mu, B. Chen, M. Zhang, Z. Guo, P. Zhang, Z. Zhang, Y. Sun, C. Shao and Y. Liu, Enhancement of the visible-light photocatalytic activity of In, *ACS Appl. Mater. Interfaces*, 2012, **1**, 424–430.

41 K. Tian, X. X. Wang, Z. Y. Yu, H. Y. Li and X. Guo, Hierarchical and hollow Fe_2O_3 nanoboxes derived from metal-organic frameworks with excellent sensitivity to H_2S, *ACS Appl. Mater. Interfaces*, 2017, **9**, 29669–29676.

42 C. N. R. Rao, *Modern Aspects of Solid State Chemistry*, Plenum Press, New York, 1970, pp. 351–353.

43 R. S. Zhao, Q. J. Bian and Q. C. Ling, *Crystallography and mineralogy*, Higher education press, Beijing, 2004, pp. 169–170.

44 P. Li, H. Q. Fan and Y. Cai, Mesoporous In_2O_3 structures: Hydrothermal synthesis and enhanced Cl_2 sensing performance, *Colloids Surf., A*, 2014, **453**, 109–116.

45 L. C. Wang, L. Y. Chen, T. Luo, K. Y. Bao and Y. T. Qian, A facile method to the cube-like $MnSe_2$ microcrystallines via a hydrothermal process, *Solid State Commun.*, 2006, **138**, 72–75.

46 J. Yang, C. X. Li, Z. W. Quan, D. Y. Kong, X. M. Zhang, P. P. Yang and J. Lin, One-Step Aqueous Solvothermal Synthesis of In_2O_3 Nanocrystals, *Cryst. Growth Des.*, 2008, **8**, 695–699.

47 A. M. Asaduzzaman, F. Y. Wang and G. Schreckenbach, Quantum-chemical study of the diffusion of Hg(0, I, II) into the ice(Ih), *J. Phys. Chem. C*, 2012, **116**, 5151–5154.

48 B. X. Xiao, S. L. Song, P. Wang, Q. Zhao, M. Y. Chuai and M. Z. Zhang, Promoting effects of Ag on In_2O_3 nanospheres of sub-ppb NO_2 detection, *Sens. Actuators, B*, 2017, **241**, 489–497.

49 Y. D. Wang, J. B. Chen and X. H. Wu, Preparation and gas-sensing properties of perovskite-type $SrFeO_3$ oxide, *Mater. Lett.*, 2001, **49**, 361–364.

50 D. Kohl, Surface processes in the detect ion of reducing gases with SnO_2-based devices, *Sens. Actuators, B*, 1989, **18**, 71–113.

51 M. H. Cao, Y. D. Wang, T. Chen, M. Antonietti and M. Niederberger, A highly sensitive and fast-responding ethanol sensor based on $CdIn_2O_4$ nanocrystals synthesized by a nonaqueous sol-gel route, *Chem. Mater.*, 2008, **20**, 5781–5786.

52 X. H. Jia, H. Q. Fan, M. Afzaal, X. Wu and P. O'Brien, Solid state synthesis of tin-doped ZnO at room temperature: Characterization and its enhanced gas sensing and photocatalytic properties, *J. Hazard. Mater.*, 2011, **193**, 194–199.

53 E. X. Chen, H. R. Fu, R. Lin, Y. X. Tan and J. Zhang, Highly selective and sensitive trimethylamine gas sensor based on cobalt imidazolate framework material, *ACS Appl. Mater. Interfaces*, 2014, **6**, 22871–22875.

54 B. X. Xiao, D. X. Wang, S. L. Song, C. B. Zhai, F. Wang and M. Z. Zhang, Fabrication of mesoporous In_2O_3 nanospheres and their ultrasensitive NO_2 sensing properties, *Sens. Actuators, B*, 2017, **248**, 519–526.

55 J. Tamaki, J. Niimi, S. Ogura and S. Konishi, Effect of micro-gap electrode on sensing properties to dilute chlorine gas of indium oxide thin film microsensors, *Sens. Actuators, B*, 2006, **117**, 353–358.